Research Square

Preprints are preliminary reports that have not undergone peer review.
They should not be considered conclusive, used to inform clinical practice,
or referenced by the media as validated information.

Molecular-scale tough adhesives based on the Lake–Thomas model

Jeong-Yun Sun

jysun@snu.ac.kr

Seoul National University https://orcid.org/0000-0002-7276-1947

Yuseon Heo

Seoul National University

Hakjun Lee

Seoul National University

Chang Seo Park

Seoul National University https://orcid.org/0000-0002-6310-5577

Jinwoo Park

Seoul National University

Seunghyun Sun

Seoul National University

Sunbo Kang

Seoul National University

Gimin Sung

Seoul National University

Yun Hyeok Lee

Massachusetts Institute of Technology https://orcid.org/0009-0002-1494-1162

Byoung Soo Kim

Korea Institute of Ceramic Engineering and Technology

Jihye Shim

Samsung Electronics

Junhyeong Park

Samsung Electronics

Article

Keywords:

Posted Date: November 17th, 2026

DOI: https://doi.org/10.21203/rs.3.rs-11438059/v1

License: This work is licensed under a Creative Commons Attribution 4.0 International License.
Read Full License

Additional Declarations: There is **NO** Competing Interest.

Title:

Molecular-scale tough adhesives based on the Lake–Thomas model

Authors:

Yuseon Heo[1†], Hakjun Lee[1†], Chang Seo Park[1], Jinwoo Park[1], Seounghyun Sun[1], Sunbo Kang[1], Gimin Sung[1], Yun Hyeok Lee[1,5], Byoung Soo Kim[2], Jihye Shim[3], Junhyeong Park[3], Jeong-Yun Sun[1,4]*

Affiliations:

[1]Department of Materials Science and Engineering, Seoul National University; Seoul 08826, Republic of Korea

[2]Bio-Convergence Materials R&D Division, Korea Institute of Ceramic Engineering and Technology; Cheongju 28160, Republic of Korea

[3]Semiconductor R&D Center, Samsung Electronics Co., Ltd.; Hwaseong-si, Gyeonggi-do 18448, Republic of Korea

[4]Research Institute of Advanced Materials (RIAM), Seoul National University; Seoul 08826, Republic of Korea

[5]Present address: Department of Materials Science and Engineering, Massachusetts Institute of Technology, Cambridge, MA 02139, USA

[†]These authors contributed equally to this work.

*Corresponding author: Jeong-Yun Sun (jysun@snu.ac.kr)

Abstract:

High interfacial fracture resistance commonly relies on finite-thickness adhesive layers that dissipate energy through deformation, whereas molecularly thin interfaces provide little volume for such toughening. We report a molecular-scale bonding strategy connecting opposing surfaces through covalently interlinked molecular bridges whose load-bearing backbone length is systematically controlled. Guided by the Lake–Thomas framework, we show that bridge backbone length controls interfacial fracture resistance through the fracture work of individual load-bearing connections. The optimized system reaches an interfacial fracture energy of approximately 500 J m^{-2} with a sub-5-nm interphase for polyimide–polyimide bonding. Surface analysis and molecular-dynamics simulations support the primary role of backbone length while suggesting that surface-tethered chain organization modulates length-dependent toughening through bridge density. The strategy strengthens dissimilar interfaces and maintains interfacial reliability under environmental exposure. In this work, we establish backbone length as a design parameter for tough molecularly thin interfaces, providing a route to mechanically robust heterogeneous integration.

Introduction

Joining dissimilar materials requires high interfacial fracture resistance. Conventional adhesive bonding achieves high fracture resistance through deformation and energy dissipation within a finite-thickness polymeric adhesive layer[1,2]. Such an interlayer, however, can introduce structural and functional discontinuities between the joined materials. This limitation is particularly relevant to integrated systems that combine dissimilar materials while preserving component geometry and function[3-6]. Molecular-scale joining strategies such as direct bonding address this dimensional constraint by minimizing or eliminating an intervening adhesive layer[7,8]. Combining a molecular-scale interfacial layer with high fracture resistance therefore remains a key challenge.

Interfacial fracture energy (G_c) comprises the intrinsic work (G_0) required to rupture load-bearing interfacial connections and additional energy dissipation (G_D) associated with material deformation[1,9]. As the interface approaches molecular dimensions, the material volume available for energy dissipation becomes highly limited[10]. The fracture work contributed by molecular connections spanning the two surfaces therefore becomes a central design consideration.

Existing molecular-scale bonding strategies have largely focused on interfacial bond density and chemistry. Surface planarization, plasma activation and wetting promote intimate contact between opposing surfaces[7,8], whereas surface-tethered molecular linkers and reactive terminal groups promote bond formation across the interface[11-15]. These approaches have established the importance of forming sufficient load-bearing connections, but have not systematically addressed how molecular architecture can increase the fracture work contributed by each connection.

The Lake–Thomas model provides a molecular-level framework for linking molecular structure to fracture energy[16,17]. In this framework, the work required to rupture each load-bearing molecular strand increases with the number of bonds along its backbone. A molecular connection that requires more work to rupture contributes more to interfacial fracture resistance. Backbone length therefore offers a molecular route to increase intrinsic interfacial fracture resistance without introducing a thick dissipative layer.

Here, we report a molecular-scale bonding strategy that connects opposing surfaces through interlinked molecular bridges and enables systematic control of their load-bearing backbone length to achieve high fracture resistance within a molecularly thin interface. This molecular control establishes backbone architecture as a design parameter for interfacial fracture resistance through the fracture work of individual load-bearing connections. The main idea is verified in a bonding between two polyimide substrates. We further apply the strategy to chemically and mechanically dissimilar interfaces and evaluate the environmental reliability of the molecularly bridged interfaces.

Results

Interlinked molecular bridges for tough molecular interfaces

To achieve high fracture resistance within a molecularly thin interface, we designed an interlinked molecular bridge system with a load-bearing backbone length that can be controlled at the molecular scale (Fig. 1). Complementary molecular nanolayers bearing amino and epoxy groups are tethered to opposing surfaces and covalently interlinked by epoxy–amine coupling to form load-bearing molecular bridges (Fig. 1a). Unlike direct bonding, which relies on local surface contact, tethered molecular chains can form covalent bridges across locally separated surface regions (Fig. 1a). This architecture enables

systematic control of the load-bearing backbone length by varying the lengths of the molecular chains tethered to each surface.

We used the Lake–Thomas model as a design principle to link this molecular architecture to fracture resistance[16,17] (Fig. 1b). In this framework, the intrinsic fracture resistance of the interface scales as

$$G_0 \propto \rho_b \cdot N_z \cdot \varepsilon \quad (1)$$

where ρ_b is areal density of molecular bridges that effectively transfer load, N_z is the number of chemical bonds in a bridge molecule and ε is the energy stored per backbone bond at fracture. The fracture work per bridge increases with N_z, making backbone bond number a molecular design parameter for controlling fracture resistance within a molecularly thin interface. We designed interlinked molecular bridges with backbone lengths ranging from N_{19} to N_{39} to examine how interfacial fracture energy varies with bridge length (Fig. 1c).

The broader adhesion landscape shows the difficulty of combining high fracture resistance with molecular-scale interfacial thickness. An Ashby plot compares interfacial fracture energy with adhesive or interphase thickness for the molecularly bridged interfaces and previously reported adhesion systems (Fig. 1d and Supplementary Table 1). Across reported adhesion systems, high fracture energies are generally achieved in thicker adhesive layers that permit bulk deformation and energy dissipation, whereas molecular-scale bonding generally combines nanometer-scale thickness with lower fracture energies. The interlinked molecular bridge system reaches an interfacial fracture energy of approximately 500 J m^{-2} at a sub-5-nm interphase thickness for PI–PI bonding (Fig. 1d). This fracture energy substantially exceeds those reported for molecular-scale bonding systems at comparable nanometer-scale thicknesses and is comparable to values achieved with micrometer-thick adhesive layers.

Backbone-length-dependent fracture of PI-PI interfaces

We implemented the interlinked molecular bridge system using 25-μm-thick polyimide (PI) films (Fig. 2a). The two PI surfaces were treated with O_2 plasma to generate hydroxyl groups and then grafted with amino-silanes A_x or glycidyl-silanes G_y, where A_x denotes amino-silane chains containing x backbone bonds (x = 9, 12, 17 and 24) and G_y denotes glycidyl-silane chains containing y backbone bonds (y = 9 and 14). We then brought the two functionalized PI surfaces into contact at 180 °C under 3 kPa for 1 h, allowing epoxy–amine coupling to form covalently interlinked molecular bridges across the interface. We denote the resulting interlinked molecular bridge containing z backbone bonds as N_z. Epoxy–amine coupling forms a new C–N bond between A_x and G_y, giving z = x + y + 1. The selected A_x and G_y combinations therefore produced bridges ranging from N_{19} to N_{39} (Fig. 2a and Supplementary Table 2). Bond counts were defined along the continuous load-bearing covalent backbone.

Interlinked molecular bridges produced a pronounced structural change at the PI–PI interface. Cross-sectional SEM showed interfacial gaps in the plasma-only control, whereas the molecularly bridged PI–PI interface remained continuous without discernible gaps (Fig. 2b). We quantified the effect of bridge backbone length on interfacial fracture resistance using 90° peel tests (Fig. 2c). The experimental configuration is shown in Supplementary Fig. 3. $N_{19} – N_{32}$ interfaces exhibited stable steady-state peel forces (Fig. 2d). The interfacial fracture energy (G_c) was calculated as $G_c = \bar{F}/w$, where $\bar{F}$ is the mean peel force measured over a displacement range of 5-30 mm and w is the specimen width. G_c varied markedly with both the presence and backbone length of the molecular bridges (Fig. 2e). The plasma-only interface showed a fracture energy of only ~3 J m^{-2}, whereas even the shortest N_{19} bridge increased G_c to ~201 J m^{-2}. This increase indicates that covalently interlinked molecular

bridges strengthen load transfer across the PI–PI interface. G_c increased monotonically from N_{19} to N_{32} with increasing backbone length, reaching a maximum of ~500 J m^{-2} for N_{32} (Fig. 2e). The PI peel arm recovered without apparent permanent curvature after peeling, and Kendall analysis estimated its extensibility contribution to be only ~0.3% of the measured fracture energy (Supplementary Fig. 5 and Note 1). From N_{19} to N_{32}, G_c broadly followed the idealized Lake–Thomas scaling at constant effective bridge density, consistent with increasing fracture work per bridge with backbone length (Fig. 2e). G_c decreased for N_{34} and N_{39} despite their longer backbones. Bridge length alone therefore does not account for the full fracture-energy dependence. We examine the molecular origin of this deviation in Fig. 3.

The N_{32} molecularly bridged interface also exhibited a distinct failure mode (Fig. 2f–k). The top-PI fracture surface exhibited extensive stretched fibrillar structures formed by deformation of the polymer matrix rather than clean debonding from the interface (Fig. 2f). Correspondingly, the bottom-PI surface contained polymer fragments transferred from the opposing PI (Fig. 2g). These fracture morphologies indicate that the interlinked load-bearing bridges strengthen the interface sufficiently to transfer the load into the adjoining PI matrix, activating cohesive deformation[18]. The chemical composition of the fracture surfaces further supports cohesive failure (Fig. 2h). Silane functionalization introduced a Si signal on PI, whereas after peeling the Si signal decreased and the overall elemental composition shifted towards that of pristine PI (Fig. 2h). The fracture surfaces therefore expose PI-rich polymer material rather than an intact silane-functionalized interface, consistent with fracture occurring within the adjoining PI. Polymer deformation and material transfer were also evident in the fracture-surface topography (Fig. 2i–k). The root-mean-square roughness increased from 6.4 nm for pristine PI to 54.7 and 25.9 nm on the top- and bottom-PI fracture surfaces, respectively. Together, the SEM, XPS and AFM results show that length-engineered molecular bridges strengthen the ultrathin interface sufficiently to shift failure

from adhesive separation to cohesive deformation and fracture within PI. The high G_c measured for N_{32} therefore reflects the fracture work of the molecularly bridged interface together with additional energy dissipation in the PI matrix.

Molecular organization of surface-tethered silanes

The decrease in G_c for N_{34} and N_{39} despite their longer backbones suggests that bridge length alone does not determine fracture resistance. We therefore examined how silane chain length affects the surface morphology and molecular organization of the surface-bound chains from which the interlinked molecular bridges are formed (Fig. 3). We used Si wafers as model substrates to characterize A_9–A_{24} amino-silane nanolayers independently of the underlying PI (Fig. 3b–h and Supplementary Fig. 8).

Surface-tethered silane chains are expected to adopt different molecular organizations depending on chain length (Fig. 3a)[19,20]. Short chains such as A_9 have relatively limited intermolecular interactions, allowing a broader range of chain tilt and conformations at the surface. Increasing chain length strengthens van der Waals interactions between neighboring hydrocarbon backbones, which can favor denser and more ordered packing with terminal amino groups remaining accessible at the outer surface[19,20]. Excessively long chains such as A_{24} have greater conformational freedom and steric interactions that can promote folding or coiling, leading to heterogeneous molecular organization and reduced terminal-group accessibility[21].

AFM revealed a chain-length dependence in the surface topography of the amino-silane nanolayers (Fig. 3b–e and Supplementary Fig. 8). A_9, A_{12} and A_{17} surfaces remained smooth with R_q values of ~0.3 nm, whereas A_{24} showed an increase in R_q to ~1.9 nm, indicating greater surface heterogeneity. XPS showed a corresponding chain-length dependence in the amino-silane nanolayers (Fig. 3f–h). The C–C and C–N components increased from A_9 to A_{17}

but decreased for A_{24} (Fig. 3f). Quantification showed the same trend, with Δ(C/Si) and Δ(N/Si) peaking at A_{17} (Fig. 3h and Supplementary Note 2). Because A_{24} contains more carbon atoms than A_{17} while retaining the same number of nitrogen atoms, its reduced C- and N-derived signals suggest lower effective surface coverage. The Si 2p spectra independently showed the same non-monotonic behavior (Fig. 3g). The substrate-derived Si^0 signal decreased from A_9 to A_{17} and increased again for A_{24}, whereas the Si^{4+}/Si^0 ratio peaked at A17 (Fig. 3h and Supplementary Note 2). G_9 and G_{14} glycidyl-silane layers remained comparatively uniform by both AFM and XPS (Supplementary Figs. 9 and 10). Effective overlayer thickness showed the same trend, increasing from ≤1 nm for A_9 to ~2–2.6 nm for A_{17} before decreasing to ≤1.2 nm for A_{24} (Supplementary Note 3).

Together, AFM and XPS are consistent with A_{17} forming a relatively extended and densely packed nanolayer, whereas A_{24} exhibits a more heterogeneous, lower-coverage organization.

Nanolayer organizations can therefore regulate effective bridge formation through surface coverage and terminal-group accessibility. This organization dependence explains the non-monotonic fracture-energy trend (Fig. 3i). Interfaces from N_{19} to N_{32}, formed with A_9–A_{17} amino-silanes, broadly follow the length-dependent Lake–Thomas scaling, reaching ~500 J m^{-2} for N_{32}. By contrast, N_{34} and N_{39} contain A_{24} and show lower fracture energies despite their longer backbones. The heterogeneous, lower-coverage A_{24} organization can reduce terminal amino-group accessibility and effective bridge formation. Backbone length determines the fracture work available from each bridge, whereas nanolayer organization limits how many effective bridges can form. The loss of surface organization at A_{24} therefore limits the length-dependent toughening expected from the Lake–Thomas picture in the longest-bridge regime.

Bridge length and density effects in molecular simulations

To distinguish the intrinsic effect of bridge length from the accompanying changes in surface population and organization, we independently varied bridge length (N_z) and brush density ρ in all-atom molecular dynamics models (Supplementary Fig. 11). The models comprised two opposing supports bearing amino-silane and glycidyl-silane brushes. After the brushes were brought into contact, epoxy-amine bonds were introduced to a target conversion of 90%. Details of the model construction, brush organization, and resulting crosslinking topologies are provided in Supplementary Figs. 12-14.

Following equilibration, the lower support was fixed and the upper support was displaced normal to the interface while the transmitted normal force was recorded. Representative configurations at equilibrium, near the maximum load-bearing state, and during progressive interfacial failure illustrate the separation process (Fig. 4a and Supplementary Fig. 15). From each force-separation curve, we extracted the maximum traction F_{max}, critical separation δ_c, and the separation work W_{sep}, by integrating the force from its onset to δ_c (Fig. 4b–c and Supplementary Figs. 16–17). F_{max} showed no systematic dependence on N_z but was consistently greater at the higher brush density (Fig. 4d). In contrast, δ_c generally increased with N_z and showed no dependency on brush density (Fig. 4e). Thus, brush density primarily determined the magnitude of the transmitted force, whereas bridge length determined the separation over which the force was sustained.

These distinct effects were combined in W_{sep}, which generally increased with N_z at both brush densities (Fig. 4f). For comparison with the experimental results, the simulated W_{sep} values were normalized and are shown in Supplementary Figs. 16-17; the corresponding absolute values are provided in Supplementary Table 3. Up to N_{32}, the experimental bridge-length dependence was consistent with the high-density simulation series, whereas the values at longer bridge lengths shifted toward the low-density series. This crossover mirrors the

changes in the population and organization of surface-tethered molecules observed in Fig. 3. Together, these results indicate that increasing bridge length enhances the work sustained by each load-bearing molecular path, whereas length-dependent changes in surface organization can offset this benefit at longer bridge lengths.

Molecularly bridged heterogeneous interfaces

We next examined whether the interlinked molecular bridge system established for the PI–PI model interface could be extended to chemically and mechanically dissimilar material pairs (Fig. 5). Si, glass, Cu and PDMS were selected as representative semiconductor, dielectric, metallic and elastomeric substrates and bonded to amino-silane-functionalized PI (Fig. 5a). G_9 and G_{14} functionalization of Si, glass, Cu and PDMS was assessed by contact-angle measurements and XPS (Supplementary Figs. 19 and 20).

Interlinked molecular bridges substantially increased fracture resistance across all heterogeneous interfaces compared with plasma-only bonding (Fig. 5b). For Si–PI, glass–PI, Cu–PI and PDMS–PI, N_{32} consistently produced higher G_c than N_{22}, showing that the bridge-length-dependent enhancement observed for PI–PI is retained across dissimilar material combinations. SEM of the paired fracture surfaces revealed distinct material-specific fracture morphologies (Fig. 5c–f). Si–PI showed dimpled plastic deformation of PI, glass–PI showed brittle glass fracture and transferred glass fragments, Cu–PI showed grain pull-out and transferred Cu grains, and PDMS–PI failed cohesively within PDMS (Fig. 5c–f). EDS confirmed material transfer across the fracture surfaces, while AFM showed increased fracture-surface roughness consistent with material-specific deformation and fracture (Supplementary Figs. 22 and 23). Together, these observations show that interlinked molecular bridges strengthen chemically and mechanically diverse interfaces sufficiently to shift failure from adhesive separation to deformation or fracture of the adjoining materials. These material-specific deformation and fracture processes can therefore contribute to the measured interfacial fracture energy.

We further evaluated the macroscopic load-bearing capability using centimeter-scale bonded specimens (Fig. 5g,h). Molecularly bridged PI–PI, Si–PI, glass–PI, Cu–PI and

PDMS–PI specimens supported applied loads of 8, 10, 10, 10 and 4 kg, respectively. At higher loads, PI–PI and PDMS–PI failed within the constituent material rather than by interfacial separation (Supplementary Fig. 24). This macroscopic demonstration shows that interlinked molecular bridges form strong load-bearing interfaces across multiple material classes rather than being restricted to a specific substrate pair.

Environmental stability of molecularly bridged interfaces

We evaluated the environmental reliability of the PI–PI interface under thermal cycling and water immersion (Fig. 6a–c). PI–PI specimens bonded with N_{22} molecular bridges retained more than 90% of their as-bonded G_c after 1,000 thermal cycles between −65°C and 150 °C, corresponding to JEDEC JESD22-A104 Test Condition C (Fig. 6a). Molecularly bridged PI–PI specimens immersed in deionized water for 30 days retained 90% of their initial G_c (Fig. 6b). Interfaces subjected to either thermal cycling or water immersion also preserved their structural integrity (Fig. 6c). Cross-sectional FIB–SEM images after 1,000 thermal cycles or 30 days of water immersion showed continuous PI–PI interfaces without obvious interfacial gaps or delamination.

We next subjected the heterogeneous interfaces established in Fig. 5 to thermal cycling between −40 and 125 °C for up to 300 cycles (JEDEC JESD22-A104 Test Condition G; Fig. 6d–h). Despite the distinct thermomechanical properties of these material pairs, all molecularly bridged interfaces retained more than 90% of their as-bonded interfacial fracture energy after 300 cycles (Fig. 6d). Cross-sectional FIB–SEM images before and after thermal cycling showed that Si–PI, glass–PI, Cu–PI and PDMS–PI interfaces remained continuous after 300 cycles without obvious interfacial separation or gaps (Fig. 6e–h). Together, these results show that interlinked molecular bridges retain high fracture resistance and structural

continuity under prolonged thermal cycling across both PI–PI and heterogeneous interfaces, while the PI–PI interface also remains stable under prolonged aqueous exposure.

Discussion

We developed an interlinked molecular bridge strategy that achieves high fracture resistance within a molecularly thin interface by engineering load-bearing molecular connections according to the Lake–Thomas framework. Increasing the bridge backbone length enhances interfacial fracture resistance by increasing the fracture work sustained by individual molecular connections. The optimized system reaches an interfacial fracture energy of approximately 500 J m^{-2} at a sub-5-nm interphase thickness for polyimide–polyimide bonding. Surface analyses and molecular-dynamics simulations show that reduced molecular organization at longer chain lengths is associated with lower effective bridge density and reduced interfacial fracture energy. The same molecular-bridging strategy applies across chemically and mechanically diverse substrate combinations, with the resulting interfaces retaining high fracture resistance under prolonged thermal cycling. Interlinked molecular bridges therefore provide a general molecular design framework for molecularly thin, mechanically robust interfaces in heterogeneous materials integration.

Methods

Materials and substrates

N-(2-Aminoethyl)-3-aminopropyltrimethoxysilane (AEPTMS, A_9; >96.0%, GC; JSI Silicon, product no. A0100.1), N-(2-aminoethyl)-6-aminohexyltrimethoxysilane (A_{12}; >96.0%, GC; JSI Silicon, product no. A0064.1), N-(2-aminoethyl)-11-aminoundecyltrimethoxysilane (A_{17}; >96.0%, GC; JSI Silicon, product no. A0120.1) and 11-[6-[N-(2-aminoethyl) amino] hexyloxy]undecyltrimethoxysilane (A_{24}; >96.0%, GC; JSI Silicon, product no. A0063.1) were used as amino-terminated silanes. 3-Aminopropyltrimethoxysilane (APTMS; >98.0%, GC; Chemical Industry, product no. A0439) was used for the model epoxy–amine coupling and temperature-dependent bonding experiments shown in Supplementary Fig. 2. 3-Glycidyloxypropyltrimethoxysilane (GPTMS, G_9; >97.0%, GC; Tokyo Chemical Industry, product no. G0210) and [8-(glycidyloxy)-*n*-octyl] trimethoxysilane (G_{14}; >97.0%, GC; Tokyo Chemical Industry, product no. G0469) were used as glycidyl-terminated silanes. The molecular nomenclature and bond-counting convention are defined below and illustrated in Fig. 2a, with the corresponding interlinked molecular-bridge designations summarized in Supplementary Table 2.

Ethanol (>95%; Duksan), acetone (>99.8%; Daejung Chemicals) and acetic acid (99.9%; Sigma-Aldrich) were used for substrate cleaning and preparation of silane solutions. Deionized water was produced using an in-house water-purification system. All chemicals were used as received unless otherwise stated.

The substrates comprised 25-μm-thick polyimide (PI) films (Kapton® 100HN, DuPont), bare Si(100) wafers (SemiRoad), 1.1 ± 0.1-mm-thick glass substrates (LK Lab Korea), Cu-coated Si wafers and 50-μm-thick polydimethylsiloxane (PDMS) films. The Cu-coated substrates comprised a 25-nm-thick Ti adhesion layer and a 200-nm-thick Cu layer deposited

sequentially onto Si wafers by sputtering (SemiRoad). PDMS films were prepared using a SYLGARD 184 Silicone Elastomer Kit (Dow). The base and curing agent were mixed at a mass ratio of 10:1, cast between spacers to obtain a film thickness of 50 μm and cured at 60 °C for 6 h. Representative atomic force microscopy topographies and the corresponding root-mean-square surface roughness values, R_q, of the pristine PI, Si, glass, Cu and PDMS substrates are provided in Supplementary Fig. 18.

Surface functionalization and interfacial bonding

Polyimide strips (1 cm × 5 cm) were used as peel arms, and the opposing PI, Si, glass, Cu and PDMS substrates measured 5.5 cm × 7.5 cm. PI samples were sonicated sequentially in ethanol and deionized water for 10 min each, immersed in acetone for 10 s and dried at 60 °C for 10 min. Si, glass and Cu substrates were sonicated in acetone for 15 min, dried under nitrogen and further dried at 60 °C for 10 min. PDMS substrates were immersed in ethanol for 3 min, gently scrubbed and dried at 60 °C for 10 min. Immediately after cleaning, the substrates were activated using a Covance-1 MPR oxygen-plasma system (FEMTO Science) at an O_2 flow rate of 65 sccm and a chamber pressure of approximately 3.0×10^{-2} Torr. PI, Si, glass and Cu were treated at 180 W for 90 s, whereas PDMS was treated at 180 W for 35 s.

Silane solutions were prepared at 2 wt% in an ethanol–water mixture (95:5, w/w). Amino-silane solutions contained no acid catalyst, whereas glycidyl-silane solutions contained 10 mM acetic acid. The solutions were stirred at 30 °C for 1 h and used immediately. Plasma-activated PI peel arms were immersed in the amino-silane solutions, and the opposing substrates were immersed in the glycidyl-silane solutions, each at 30 °C for 30 min. Functionalized PI, Si, glass and Cu samples were rinsed sequentially with ethanol and deionized water for 1 min each and gently scrubbed with acetone. PDMS samples were rinsed

identically without acetone scrubbing. All samples were dried under nitrogen, further dried at 60 °C for 10 min and bonded immediately.

The subscripts x and y in A_x and G_y denote the numbers of covalent bonds along the continuous load-bearing paths from the substrate surface to the terminal amino group and reactive epoxide carbon, respectively, including the surface–O and O–Si bonds. Epoxy–amine coupling forms an interlinked molecular bridge, N_z, containing z backbone bonds, where z = x + y + 1. The additional bond corresponds to the newly formed C–N bond. The silane combinations used to form each N_z bridge are summarized in Supplementary Table 2.

Complementary functionalized surfaces were brought into contact and gently rolled to remove trapped air. The assembled specimens were then held under vacuum for 10 min before thermal bonding. A dead weight corresponding to 3 kPa over the 1 cm × 5 cm bonded area was applied during thermal bonding. PI–PI, Si–PI, glass–PI and Cu–PI interfaces were bonded at 180 °C for 1 h, whereas PDMS–PI interfaces were bonded at 90 °C for 1 h. The applied pressure was maintained during natural cooling to room temperature. Plasma-only controls were prepared using the same cleaning, plasma activation, assembly and thermal-bonding procedures without silane functionalization.

Contact-angle measurement

Static water contact angles were measured under ambient conditions using a SD-standard, Femtobiomed by the sessile-drop method. A 3-µl droplet of deionized water was placed on each surface, and the contact angle was determined from the droplet profile. For PI, measurements were performed on pristine, O_2-plasma-treated and silane-functionalized surfaces, including A_9-, A_{12}-, A_{17}-, A_{24}-, G_9- and G_{14}-functionalized PI (Supplementary Fig. 1). For the heterogeneous substrates, pristine, O_2-plasma-treated and G_9- or G_{14}-functionalized Si, glass, Cu and PDMS surfaces were analyzed to assess the surface changes

associated with glycidyl-silane functionalization (Supplementary Fig. 19). Contact angles were measured at three spatially separated positions for each condition and are reported as mean ± s.d.

FT-IR analysis and temperature-dependent bonding

Epoxy–amine coupling was examined using a substrate-free model system comprising 3-aminopropyltrimethoxysilane (APTMS) and 3-glycidyloxypropyltrimethoxysilane (GPTMS). APTMS and GPTMS were mixed at a 1:1 molar ratio without solvent. For the temperature-dependent measurements, the mixtures were reacted for 60 min at 60, 90, 120, 150, 165, 180 or 195 °C. For the time-dependent measurements, the mixtures were reacted at 180 °C for 0, 30, 60, 90 or 120 min.

Fourier-transform infrared (FT-IR) spectra were acquired using a Nicolet iS50, Thermo Fisher Scientific in attenuated total reflection (ATR) mode over 400–4,000 cm^{-1} using 32 scans per spectrum. Spectra were baseline-corrected before analysis. Reaction progress was evaluated from changes in the C–N and epoxy-ring bands. For the temperature series, the C–N band at 1,240 cm^{-1} and epoxy-ring band at 630 cm^{-1} were analyzed, whereas the C–N band at 1,470 cm^{-1} and epoxy-ring band at 630 cm^{-1} were analyzed for the time series. The corresponding band intensities were normalized to the values measured at 60 °C for the temperature series and at 0 min for the time series.

For temperature-dependent PI–PI bonding experiments, PI surfaces functionalized with APTMS and GPTMS were prepared and assembled using the same surface-treatment and bonding procedures described above. The interfaces were bonded under 3 kPa for 1 h at 60, 90, 120, 150 or 180 °C. Interfacial fracture energy was measured by 90° peel testing as described below.

X-ray photoelectron spectroscopy

X-ray photoelectron spectroscopy (XPS) was performed using a VersaProbe III system (ULVAC–PHI) equipped with a monochromated Al Kα X-ray source ($h\nu = 1{,}486.6$ eV). Survey spectra were acquired at a pass energy of 224 eV, and high-resolution spectra were acquired at 55 eV, except for the Si 2p spectra, which were acquired at 112 eV. Binding energies were charge-corrected by setting the adventitious carbon C 1s peak to 284.8 eV. Measurements were collected at three randomly selected positions on each surface at a photoelectron take-off angle of 45° relative to the sample surface, without ion sputtering. Spectra were processed using MultiPak software.

XPS was used to characterize pristine and silane-functionalized surfaces. Chain-length-dependent changes in the amino-silane layers were evaluated using bare Si and A_9-, A_{12}-, A_{17}- and A_{24}-functionalized Si surfaces. Si was selected as a model substrate because its low C and N background and well-defined substrate Si^0 signal enabled comparison of the silane-containing overlayers. G_9- and G_{14}-functionalized Si, glass, Cu and PDMS surfaces were also analyzed to assess glycidyl-silane functionalization across the different substrates. For the PI surfaces, C 1s, N 1s, O 1s and Si 2p spectra were acquired as appropriate for each surface. Pristine PI, A_{17}- and G_{14}-functionalized PI, and the top and bottom fracture surfaces of N_{32}-bonded PI–PI interfaces were also analyzed to examine changes in surface composition after fracture.

Elemental compositions were obtained from the survey spectra using the relative sensitivity factors implemented in MultiPak. High-resolution spectra were fitted to analyze the silane-derived chemical states and the relative contributions of substrate Si^0 and oxidized Si^{4+} species. The procedures used to calculate Δ(C/Si), Δ(N/Si) and the Si^{4+}/Si^0 peak-area ratio are

described in Supplementary Note 2. Estimation of the XPS-derived effective silane-overlayer thickness using the MultiPak attenuation model is described in Supplementary Note 3.

Atomic force microscopy

Atomic force microscopy (AFM) was performed using a Cypher system (Asylum Research, Oxford Instruments) in tapping mode under ambient conditions with PR-T300 cantilevers. Images were acquired at scan rates of 0.8–1.2 Hz and a resolution of 512 x 512 pixels. Pristine PI, Si, glass, Cu and PDMS surfaces were analyzed to determine their initial surface topography and root-mean-square roughness, R_q(Supplementary Fig. 18). Surface topography of the amino-silane nanolayers was examined on Si surfaces functionalized with A_9, A_{17} and A_{24}, with bare Si included as a reference (Fig. 3b–e). The corresponding A_{12}-functionalized Si surface is shown in Supplementary Fig. 8. Glycidyl-silane nanolayers were examined on Si surfaces functionalized with G_9 and G_{14} (Supplementary Fig. 9). Following 90° peel testing of N_{32}-bonded interfaces, the opposing fracture surfaces of PI–PI, Si–PI, glass–PI, Cu–PI and PDMS–PI specimens were analyzed to characterize fracture-induced changes in surface topography and roughness (Fig. 2i–k and Supplementary Fig. 23). The R_q values were calculated directly from the acquired height data without image flattening.

Interfacial fracture energy measurements

Interfacial fracture energies were measured by 90° peel testing using an Instron 3343 universal testing machine (Instron) equipped with a 1-kN load cell and a peel-test fixture. A 25-μm-thick PI film was used as the peel arm, whereas the opposing PI, Si, glass, Cu or PDMS substrate was fixed horizontally to the lower stage. Specimens with a bonded width of 10 mm were tested at room temperature at a crosshead speed of 10 mm min^{-1}. The interfacial fracture energy, G_c, was calculated as $G_c = \bar{F}/w$, where $\bar{F}$ is the mean steady-state peel force

measured over a displacement range of 5–30 mm and w is the bonded specimen width. Five independently prepared specimens were tested for each condition, except for N_{27}, for which ten specimens were tested (n = 5 for each of the A_{17}/G_9 and A_{12}/G_{14} combinations). The experimental configuration is shown in Supplementary Fig. 3. The contribution of peel-arm extensibility to the measured fracture energy was evaluated separately using the Kendall peel model[22] (Supplementary Note 1).

Static shear load-bearing tests

The static shear load-bearing capability of N_{32}-bridged interfaces was evaluated using PI–PI, Si–PI, glass–PI, Cu–PI and PDMS–PI specimens with a bonded area of 3 cm × 3 cm. One side of each bonded specimen was fixed, and dead weights were suspended from the opposite side such that the applied load acted predominantly parallel to the bonded interface. Loads of 4, 6, 8 and 10 kg were applied sequentially for 1 min each at room temperature as an initial screening test. The highest screening load sustained without failure was then maintained for 1 h. The corresponding sustained loads were 8, 10, 10, 10 and 4 kg for PI–PI, Si–PI, glass–PI, Cu–PI and PDMS–PI interfaces, respectively.

Electron microscopy and elemental analysis

Scanning electron microscopy (SEM), energy-dispersive X-ray spectroscopy (EDS) and focused ion beam (FIB) sectioning were performed using an AURIGA CrossBeam system (ZEISS) equipped with a FlatQUAD EDS detector. Pristine PI, Si, glass, Cu and PDMS surfaces were imaged as references for comparison with the corresponding fracture surfaces. Following 90° peel testing, both opposing fracture surfaces of N32-bonded PI–PI, Si–PI, glass–PI, Cu–PI and PDMS–PI interfaces were imaged at an accelerating voltage of 5 kV using an InLens detector. EDS spectra and elemental maps were acquired at 5 kV to assess material transfer between the opposing fracture surfaces.

Cross-sectional SEM images of the as-bonded PI–PI interfaces shown in Fig. 2b were obtained from specimens cooled in liquid nitrogen and fractured normal to the bonded interface. For reliability analysis, as-bonded specimens and specimens subjected to thermal cycling or water immersion were sectioned normal to the bonded interface by FIB milling using the same system. The prepared cross sections were subsequently imaged by SEM to examine interfacial morphology and continuity.

Thermal cycling and water immersion

PI–PI specimens were subjected to thermal cycling between −65°C and 150 °C for 1, 10, 500 or 1,000 cycles. Each cycle comprised a dwell time of 13.6 min at each temperature limit, with transitions between the two limits completed within approximately 3.4 min. Separate PI–PI specimens were immersed in deionized water at 25 ℃ for 1, 7, 14, 30 days. After immersion, residual surface water was removed, and the specimens were dried at 60 °C for 10 min before 90° peel testing.

Si–PI, glass–PI, Cu–PI and PDMS–PI specimens were thermally cycled between −40°C and 125 °C for 100, 200 or 300 cycles using the same dwell and transition conditions. Interfacial fracture energies were measured by 90° peel testing after each treatment condition as described above. Five independently prepared specimens were tested for each condition. For FIB–SEM analysis, representative cross sections were prepared from the specimens exposed to the maximum treatment conditions, including PI–PI interfaces after 1,000 thermal cycles or 30 days of water immersion and dissimilar interfaces after 300 thermal cycles. As-bonded specimens were analyzed as untreated references.

Adhesion performance map

The adhesion performance map was constructed from previously reported bonding and adhesive systems for which both an energy-based adhesion or fracture metric and the corresponding adhesive or interphase thickness were quantitatively available. Fracture-energy values obtained from peel, double-cantilever-beam (DCB) or related energy-based fracture measurements were converted to J m^{-2}, and thickness values were converted to metre for plotting. Numerical values were taken from the original reports or, when available only graphically, estimated from the published figures.

Literature systems were classified according to the dominant interfacial attachment mechanism as chemical-bond-mediated or physical-interaction-mediated adhesion. Chemical-bond-mediated systems involved intentional covalent or other primary chemical bonds across the bonded interface, whereas physical-interaction-mediated systems relied predominantly on noncovalent interactions such as hydrogen bonding, van der Waals interactions, polar interactions or wetting.

Lines of constant thickness-normalized fracture energy were calculated as $G_c/t = C$ where C is expressed in J m^{-3}. For the present work, G_c values for PI–PI, Si–PI, glass–PI, Cu–PI and PDMS–PI interfaces were obtained from 90° peel measurements. For plotting, an effective interphase thickness of approximately 3.2 nm for N_{32}, estimated from XPS-derived effective overlayer thicknesses of the complementary silane layers, was assigned to all substrate combinations. The literature sources, interfacial classifications and numerical values are summarized in Supplementary Table 1.

Molecular model construction and brush equilibration

Molecular dynamics (MD) simulations were performed using the Large-scale Atomic/Molecular Massively Parallel Simulator (LAMMPS) with the polymer consistent force field (PCFF) [23, 24]. Periodic boundary conditions were applied along the x- and y-

directions, whereas nonperiodic fixed boundaries were applied along the z-direction. A vacuum region of 150 Å was included along the z-axis to allow complete interfacial separation. The lateral dimensions were fixed at Lx=38.4 Å and Ly=33.3 Å for all molecular models.

The interfacial model consisted of two opposing rigid Si (111) support layers bearing amino-silane and glycidyl-silane brushes, respectively. Each support was treated as a rigid body, with its internal geometry and connectivity held fixed throughout the simulations. Nonbonded interactions between the Si support atoms and the organic region were excluded, such that the support served only as rigid anchoring bodies. Each brush molecule was attached to the corresponding Si support through a single anchoring bond.

Different amino- and glycidyl-silane combinations were used to vary the bridge length, N, defined as the number of backbone bonds along the molecular load-bearing path connecting the two supports. The nominal brush density, ρ, was varied by occupying 25 or 50 of the 100 available anchoring sites, corresponding to ρ_L = 1.96 sites nm^{-2} and ρ_H = 3.92 sites nm^{-2}, respectively. The initial separation between the supports was adjusted for each molecular combination to obtain a nominal density of approximately 1.0g cm^{-3} within the confined organic region.

Before interfacial crosslinking, the uncrosslinked brush configurations were equilibrated with both supporting fixed. The density-dependent brush orientation was quantified using the tilt angle. The geometric definition of tilt angle and the corresponding angle distributions are provided in Supplementary Fig. 12.

Interfacial crosslinking and reaction-template mappings

Pre- and post-reaction templates for epoxy–amine crosslinking and covalent-bond scission were prepared using the REACTER framework. The LUNAR toolkit was used to assign the

corresponding PCFF parameters and generate atom mappings between the pre- and post-reaction states[25,26]. The resulting templates and mapping files were implemented in LAMMPS through the fix bond/react command for both crosslink formation and subsequent bond scission.

For interfacial crosslinking, the opposing brush layers were placed in the compact interfacial configurations described above. Candidate epoxy–amine reaction sites were identified using a distance-based criterion, and the reaction cutoff was progressively increased until a target conversion of approximately 90% was reached. The multifunctional amino-silanes could participate in multiple epoxy–amine reactions, producing connection topologies beyond simple one-to-one brush pairs. The reaction templates, cutoff procedure and crosslinking workflow are provided in Supplementary Fig. 13. Surface-spanning bridges were identified by tracing the molecular connectivity between brush molecules anchored to the opposing Si supports. The surface-spanning fraction was quantified for each bridge-length and brush-density condition. The bridge-counting criterion and classification of the resulting connection topologies are provided in Supplementary Fig. 14.

The crosslinked structures were subsequently energy-minimized with both Si supports fixed. The organic region was equilibrated at 298 K using a Langevin thermostat with a damping constant of 100 fs and an nve/ limit integrator with a maximum atomic displacement of 0.1 Å per timestep. A timestep of 0.05 fs was used, and equilibration was performed for 60 ps. The equilibrated structures were used as the initial configurations for the subsequent separation simulations.

Traction–separation simulations and failure analysis

Traction–separation simulations were performed by fixing the lower Si support and translating the upper support as a rigid body along the positive z-direction at a constant

569 velocity of 1.0×10^{-4} Å / fs. The equations of motion for the organic atoms were integrated
570 using fix nve with a timestep of 0.05fs, while their temperature was maintained at 298K using
571 a Langevin thermostat. Each simulation lasted 750ps, corresponding to a total imposed
572 increase in support separation of 75 Å.

573 Covalent-bond scission was implemented as a predefined reaction through fix bond/react
574 using the LUNAR-generated pre- and post-scission templates. A scission reaction was
575 triggered when a breakable bond exceeded approximately 1.5 times its equilibrium bond
576 length. The bond-specific rupture distances ranged from 2.130 to 2.849 Å. Identical scission
577 criteria were applied to all bridge-length and brush-density conditions.

578 The instantaneous support separation was calculated as the z-direction distance between the
579 centers of mass of the upper and lower Si supports. The normal force, F, was obtained by
580 summing the z-direction forces acting on the atoms of the upper support, with positive values
581 defined in tension. Force and separation were sampled every 10 timesteps and averaged over
582 250 consecutive samples, giving an output interval of 0.125 ps.

583 The separation, δ, was referenced to the onset of sustained tensile force by subtracting the
584 support separation at the force onset from the instantaneous support separation. The
585 maximum force, F_{max}, was defined as the maximum normal force during separation. The
586 critical separation, δ_c ,was defined as the first post-peak displacement at which the force
587 decreased below 1% of F_{max} and remained below this threshold. The work of separation,
588 W_{sep}, was calculated as

589 $$W_{sep} = \frac{\int_0^{\delta_c} F(\delta) d\delta}{A}$$

590 where A is the area of the xy-plane of the simulated cell. Unless otherwise stated, identical
591 simulation and analysis procedures were applied to all bridge-length and surface-coverage

conditions. Complete traction–separation curves are provided in the Supplementary Figure 16 and 17.

Data availability

The data supporting the findings of this study are available within the paper and its Supplementary Information. Additional data are available from the corresponding author upon reasonable request.

Code availability

No custom simulation software or novel computational algorithms were developed in this study. Molecular dynamics simulations were performed using LAMMPS (version 29 Aug 2024). The simulation protocols, force-field parameters, and analysis procedures are described in the Methods and Supplementary Information.

References

1. Yuk, H., Zhang, T., Lin, S., Parada, G. A. & Zhao, X. Tough bonding of hydrogels to diverse non-porous surfaces. *Nat. Mater.* **15**, 190–196 (2016).

2. Li, J. *et al.* Tough adhesives for diverse wet surfaces. *Science* **357**, 378–381 (2017).

3. Mahajan, R. V. *et al.* The heterogeneous integration of electronic components. *Nat. Rev. Electr. Eng.* **3**, 254–263 (2026).

4. Liu, Y., Huang, Y. & Duan, X. Van der Waals integration before and beyond two-dimensional materials. *Nature* **567**, 323–333 (2019).

5. Shekhar, S. *et al.* Roadmapping the next generation of silicon photonics. *Nat. Commun.* **15**, 751 (2024).

6. Churaev, M. *et al.* A heterogeneously integrated lithium niobate-on-silicon nitride photonic platform. *Nat. Commun.* **14**, 3499 (2023).

7. Chew, S. A., De Vos, J. & Beyne, E. Wafer-to-wafer hybrid bonding at 400-nm interconnect pitch. *Nat. Rev. Electr. Eng.* **1**, 71–72 (2024).

8. Moutanabbir, O. & Gösele, U. Heterogeneous integration of compound semiconductors. *Annu. Rev. Mater. Res.* 40, 469–500 (2010).

9. Gent, A. N. & Lai, S.-M. Interfacial bonding, energy dissipation, and adhesion. *J. Polym. Sci. B Polym. Phys.* **32**, 1543–1555 (1994).

10. Isaacson, S. G. *et al.* Fundamental limits of material toughening in molecularly confined polymers. *Nat. Mater.* **15**, 294–298 (2016).

11. Gösele, U., Steinnkirchner, J., Martini, T., Reiche, M. & Kästner, G. Silicon wafer bonding via designed monolayers. *Adv. Mater.* **7**, 662–665 (1995).

12. Ramanath, G. *et al.* Self-assembled subnanolayers as interfacial adhesion enhancers and diffusion barriers for integrated circuits. *Appl. Phys. Lett.* **83**, 383–385 (2003).

13. Gandhi, D. D. *et al.* Annealing-induced interfacial toughening using a molecular nanolayer. *Nature* **447**, 299–302 (2007).

14. O'Brien, P. J. *et al.* Bonding-induced thermal conductance enhancement at inorganic heterointerfaces using nanomolecular monolayers. *Nat. Mater.* **12**, 118–122 (2013).

15. Ramanath, G. *et al.* Engineering inorganic interfaces using molecular nanolayers. *Appl. Phys. Lett.* **122**, 260502 (2023).

16. Lake, G. J. & Thomas, A. G. The strength of highly elastic materials. *Proc. R. Soc. Lond. A* 300, 108–119 (1967).

17. Wang, S., Panyukov, S., Rubinstein, M. & Craig, S. L. Quantitative adjustment to the molecular energy parameter in the Lake–Thomas theory of polymer fracture energy. *Macromole*

cules **52**, 2772–2777 (2019).

18. Kwan, M. *et al.* Frequency-tunable toughening in a polymer-metal-ceramic stack using a n interfacial molecular nanolayer. *Nat. Commun.* **9**, 5249 (2018).

19. Xiao, X., Hu, J., Charych, D. H. & Salmeron, M. Chain length dependence of the friction al properties of alkylsilane molecules self-assembled on mica studied by atomic force micros copy. *Langmuir* **12**, 235–237 (1996).

20. Khatri, O. P., Bain, C. D. & Biswas, S. K. Effects of chain length and heat treatment on t he nanotribology of alkylsilane monolayers self-assembled on a rough aluminum surface. *J. P hys. Chem. B* **109**, 23405–23414 (2005).

21. Sambasivan, S., Hsieh, S., Fischer, D. A. & Hsu, S. M. Effect of self-assembled monolayer film order on nanofriction. *J. Vac. Sci. Technol.* A **24**, 1484–1488 (2006).

22. Kendall, K. Thin-film peeling—the elastic term. *J. Phys. D Appl. Phys.* **8**, 1449–1452 (1975).

23. Plimpton, S. Fast parallel algorithms for short-range molecular dynamics. *J. Comput. Phys.* **117**, 1–19 (1995).

24. Sun, H., Mumby, S. J., Maple, J. R. & Hagler, A. T. An ab initio CFF93 all-atom force field for polycarbonates. *J. Am. Chem. Soc.* **116**, 2978–2987 (1994).

25. Gissinger, J. R., Jensen, B. D. & Wise, K. E. REACTER: A heuristic method for reactive molecular dynamics. *Macromolecules* **53**, 9953–9961 (2020).

26. Kemppainen, J., Gissinger, J. R., Gowtham, S. & Odegard, G. M. LUNAR: Automated input generation and analysis for reactive LAMMPS simulations. *J. Chem. Inf. Model.* **64**, 5108–5126 (2024).

27. Olbrechts, B., Zhang, X., Bertholet, Y., Pardoen, T. & Raskin, J.-P. Effect of interfacial SiO_2 thickness for low temperature O_2 plasma activated wafer bonding. *Microsyst. Technol.* **12**, 383–390 (2006).

28. Liang, D. et al. Low-temperature, strong SiO_2–SiO_2 covalent wafer bonding for III–V compound semiconductors-to-silicon photonic integrated circuits. *J. Electron. Mater.* **37**, 1552–1559 (2008).

29. Tong, Q.-Y., Gan, Q., Hudson, G., Fountain, G. & Enquist, P. Low temperature InP/Si wafer bonding. *Appl. Phys. Lett.* **84**, 732–734 (2004).

30. Kwon, Y., Seok, J., Lu, J. Q., Cale, T. S. & Gutmann, R. J. Critical adhesion energy of benzocyclobutene-bonded wafers. *J. Electrochem. Soc.* **153**, G347–G352 (2006).

31. Sim, G. D., Chung, C. K., Paik, K. W. & Lee, S. B. Moisture induced interface weakening in ACF package. *Mater. Sci. Eng. A* **528**, 698–705 (2010).

673 32. Wan, Y., Yin, Q., Zhang, P., Yang, C. & Bai, R. Interfacial fatigue fracture of pressure
674 sensitive adhesives. *Extreme Mech. Lett.* **72**, 102248 (2024).

675 33. Grzelka, M., Kooij, S., Woutersen, S., Adda-Bedia, M. & Bonn, D. Transition from
676 viscoelastic to fracture-like peeling of pressure-sensitive adhesives. *Soft Matter* **18**, 999–1004
677 (2022).

678 34. Villey, R. et al. Rate-dependent elastic hysteresis during the peeling of pressure sensitive
679 adhesives. *Soft Matter* **11**, 3480–3491 (2015).

680 35. Pandey, V., Fleury, A., Villey, R., Creton, C. & Ciccotti, M. Linking peel and tack
681 performances of pressure sensitive adhesives. *Soft Matter* **16**, 3267–3275 (2020).

682 36. Du, Q. et al. Self-compliant ionic nanomesh for gas-permeable and stress-free on-skin
683 electronics. *Nat. Commun.* **16**, 11510 (2025).

684 37. Zhang, P., Ruan, H., Li, Q., He, Y. & Yang, C. Resolving hyperelasticity-adhesiveness
685 conflict in polymer networks by in situ constructing mechanical heterogeneities. *Nat.*
686 *Commun.* **16**, 6094 (2025).

687 38. Yang, Q. et al. Photocurable bioresorbable adhesives as functional interfaces between
688 flexible bioelectronic devices and soft biological tissues. *Nat. Mater.* **20**, 1559–1570 (2021).

689 39. Liu, J. et al. Fatigue-resistant adhesion of hydrogels. *Nat. Commun.* **11**, 1071 (2020).

690 40. Wang, Y. et al. Instant, tough, noncovalent adhesion. *ACS Appl. Mater. Interfaces* **11**,
691 40749–40757 (2019).

692 41. Yi, B. et al. Surface hydrophobization of hydrogels via interface dynamics-induced
693 network reconfiguration. *Nat. Commun.* **15**, 239 (2024).

694 42. Xie, W. et al. Organohydrogel-based transparent terahertz absorber via ionic conduction
695 loss. *Nat. Commun.* **15**, 38 (2024).

696

Acknowledgements

The Institute of Engineering Research at Seoul National University provided research facilities for this work.

Funding

This research was supported by National Research Foundation of Korea (NRF) grants funded by the Korean government (grant numbers RS-2026-25607756 and RS-2026-25618652 to J.-Y.S.) and Samsung Electronics' University R&D program.

Author contributions

Y.H. conceived the idea, designed and performed the experiments, and analyzed the experimental results. H.L. conducted the molecular dynamics simulations and analyzed the simulation results. Y.H. and H.L. interpreted the results. C.S.P. contributed to the molecular dynamics simulations and analysis. J.W.P. assisted with the thermal cycling experiments. S.K. and G.S. assisted with the experimental procedures. S.S., Y.H.L., B.S.K., J.S. and J.H.P. provided advice on revising the manuscript. Y.H., H.L. and J.-Y.S. wrote and revised the manuscript. J.-Y.S. contributed to the conceptual development and supervised the study.

Competing interests

The authors declare no competing interests.

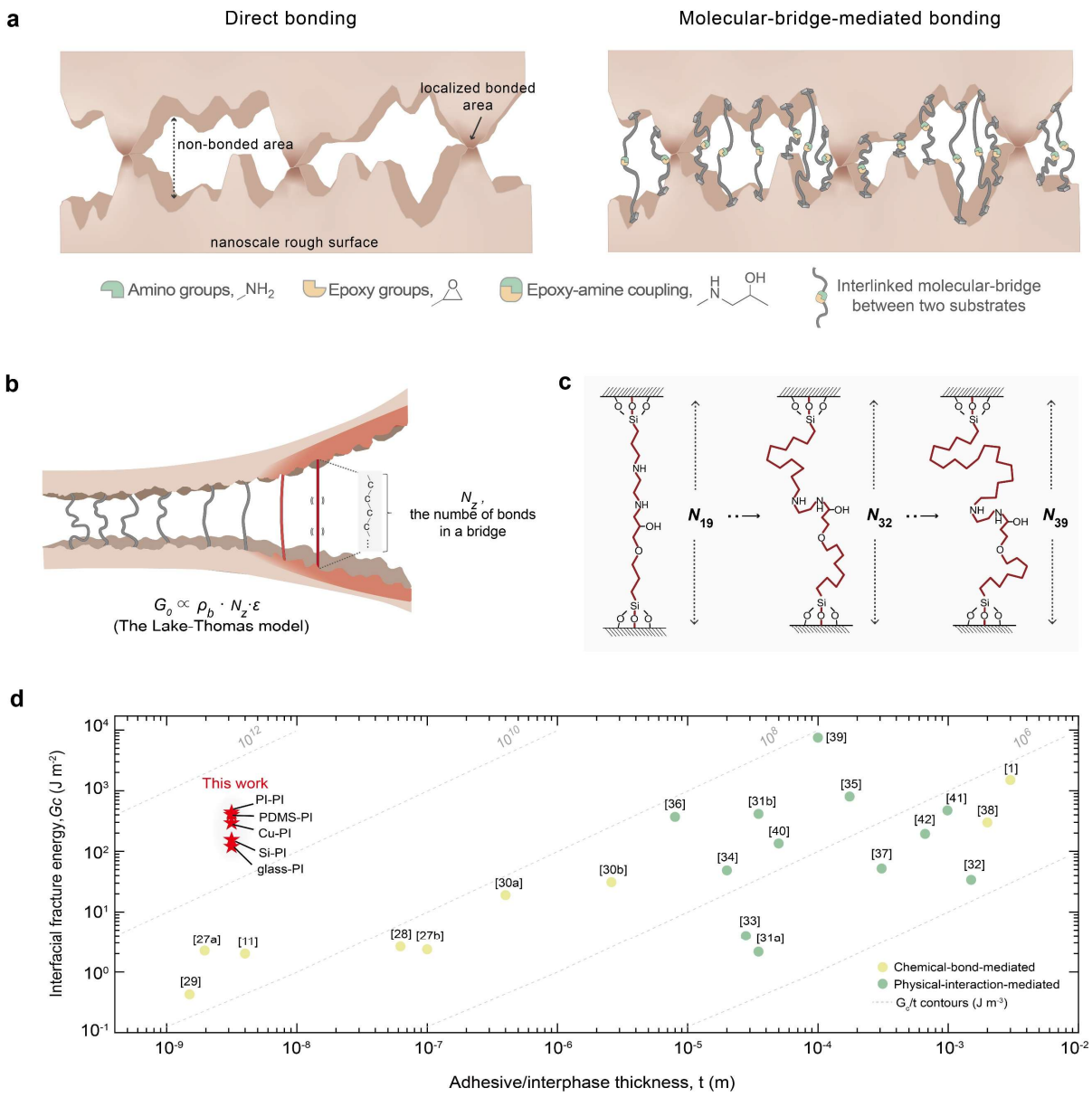


Fig. 1 | Molecularly thin and tough adhesives based on the Lake-Thomas model

a, Schematic comparison with direct bonding and molecular-bridge-mediated bonding between nanoscale-rough surfaces. Surface roughness limits intimate contact in direct bonding, localizing the bonded regions, whereas tethered molecular chains can form covalent bridges across locally separated surface regions. **b,** Intrinsic work of fracture (G_0) of the interlinked molecular bridges can be interpreted using Lake-Thomas model. G_0 is proportional to the number of bonds in a bridge (N_z). **c,** The interlinked molecular bridges range from N_{19} to N_{39}. Representative structures of N_{19}, N_{32} and N_{39} are shown. **d,** Ashby plot

of interfacial fracture energy (G_c) versus adhesive/interphase thickness (t). The interfaces were classified as ‘chemical-bond-mediated’ or ‘physical-interaction-mediated’ according to their mechanism. Red stars indicate PI–PI, Si–PI, glass–PI, Cu–PI and PDMS–PI interfaces formed with N_{32} interlinked molecular bridges. An effective interphase thickness of approximately 3.2 nm, estimated from XPS-derived overlayer thicknesses for N_{32}, was used for the present work. Dashed diagonal lines indicate the interfacial fracture energy normalized by the thickness (Gc/t) (J m^{-3}).

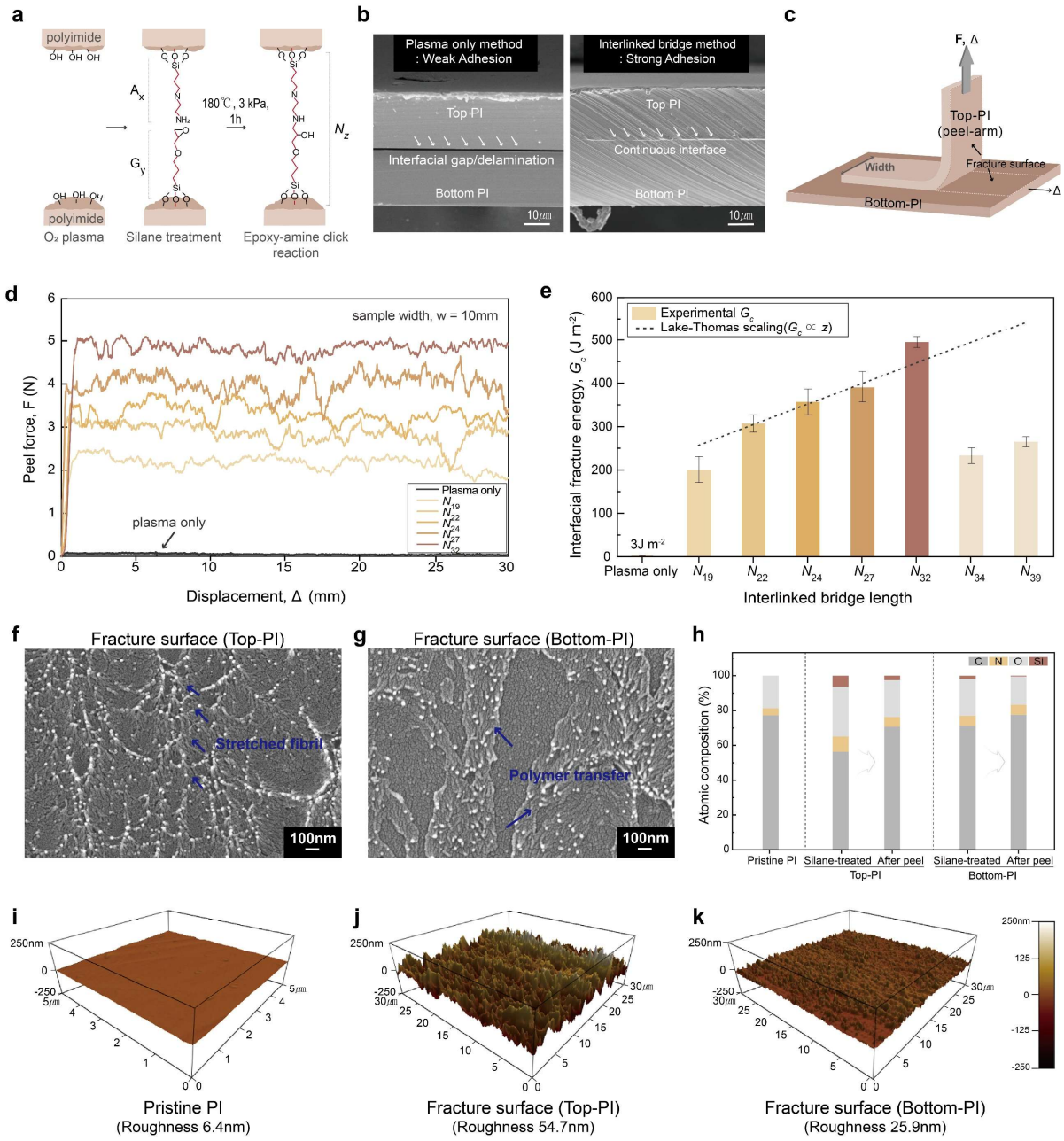


Fig. 2 | Bonding process and fracture behavior of molecularly bridged PI–PI interfaces. **a,** Process of the molecular-bridge-mediated bonding. Top and bottom polyimide (PI) films were activated by oxygen plasma, then functionalized with amino-silane chains (A_x) and glycidyl-silane chains (G_y) respectively, where x and y denote the numbers of backbone bonds. The interlinked molecular bridge (N_z) with z = x+y+1 is formed by epoxy-amine click reaction at 180 °C under 3 kPa for 1 h. **b,** Cross-sectional SEM images of plasma-only and

molecular-bridged PI-PI interfaces. The plasma-only sample was bonded immediately after oxygen-plasma treatment under the same bonding conditions. **c,** Schematic of 90° peel test used to measure interfacial fracture energy. Representative 90° peel tests of the plasma-only and N_{32} interfaces are shown in Supplementary Movies 1 and 2. **d,** Representative peel-force vs displacement curves of the plasma-only and N_{19}-N_{32} PI–PI interfaces. Representative N_{34} and N_{39} curves are shown in Supplementary Fig. 4. **e,** Interfacial fracture energy (G_c) as a function of bridge backbone length. The dashed line represents Lake–Thomas scaling with N_{24} value. Data are presented as mean ± s.d. (n=5, except N_{27}, n=10). **f,g,** SEM images of the fractured top-PI and bottom-PI surfaces, showing stretched polymer fibrils and transferred PI, respectively. SEM image of pristine PI is shown in Supplementary Fig. 6. **h,** Atomic composition (C, N, O and Si) is measured with XPS at the surfaces of pristine PI, the amino-silane-treated top-PI and glycidyl-silane-treated bottom-PI before bonding, and the corresponding fracture surfaces after peeling of the N_{32} interface. Bars represent mean atomic percentages from three measurements at different positions in a sample. **i–k,** AFM topographies of the pristine PI, the fractured top-PI and the fractured bottom-PI, respectively. The corresponding root-mean-square roughness values (R_q) are 6.4, 54.7 and 25.9 nm, respectively. Corresponding two-dimensional AFM height images are shown in Supplementary Fig. 7.

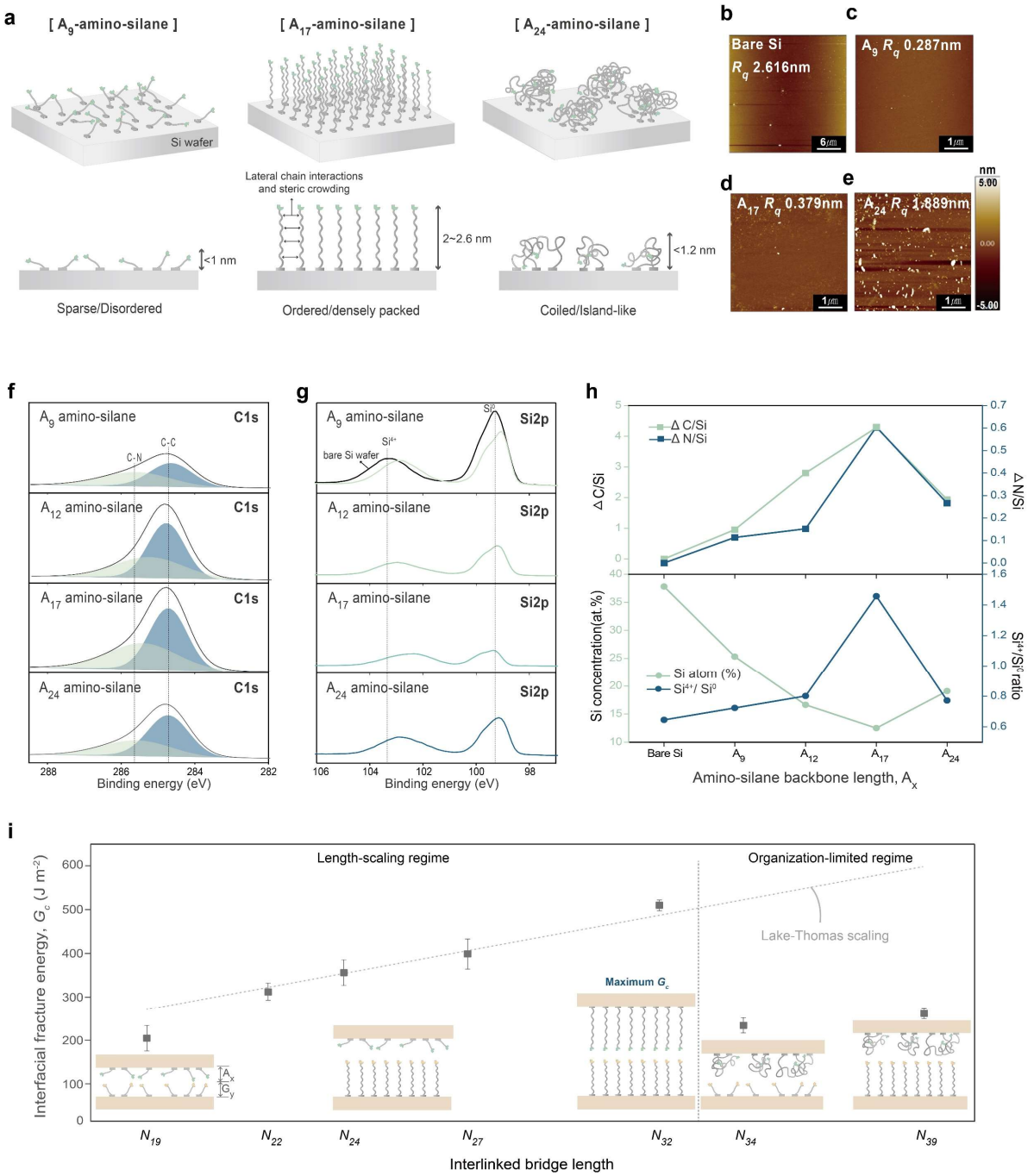


Fig. 3 | Chain-length-dependent surface morphology and interfacial toughness

a, Proposed model of chain-length-dependent surface morphology grafted by amino-silane chains on Si wafers. A_9, A_{17} and A_{24} represent short, intermediate and long amino-silane chains, respectively, with proposed sparse/disordered, ordered/densely packed and coiled/island-like organizations. The indicated effective overlayer thicknesses were estimated from XPS analysis (Supplementary Note 3). Si wafers were used as model substrates for

surface characterization. **b–e,** AFM topographies of (b) bare Si and Si surfaces functionalized with (c) A_9, (d) A_{17} and (e) A_{24} amino-silane chains, respectively. The AFM topography of A_{12}-functionalized Si is shown in Supplementary Fig. 8. **f,** High-resolution C 1s X-ray photoelectron spectra of Si wafers functionalized with A_9, A_{12}, A_{17} and A_{24} amino silanes, showing chain-length-dependent C–C and C–N contributions. **g**, Corresponding Si 2p spectra showing contributions from substrate Si^0 and oxidized Si^{4+} species associated with the surface oxide and silane-containing overlayer. **h,** Quantitative analysis of the XPS spectra in **f** and **g**, showing Δ(C/Si) and Δ(N/Si) relative to bare Si, total Si atomic concentration and the Si^{4+}/Si^0 peak-area ratio as functions of amino-silane backbone length. **i**, Mechanistic summary for a linkage between chain-length-dependent surface morphology and interfacial fracture energy. Interfaces from N_{19}– N_{32} broadly follow Lake–Thomas scaling, whereas N_{34} and N_{39} deviate from this trend, likely because the coiled/island-like organization of A_{24} limits effective bridge formation.

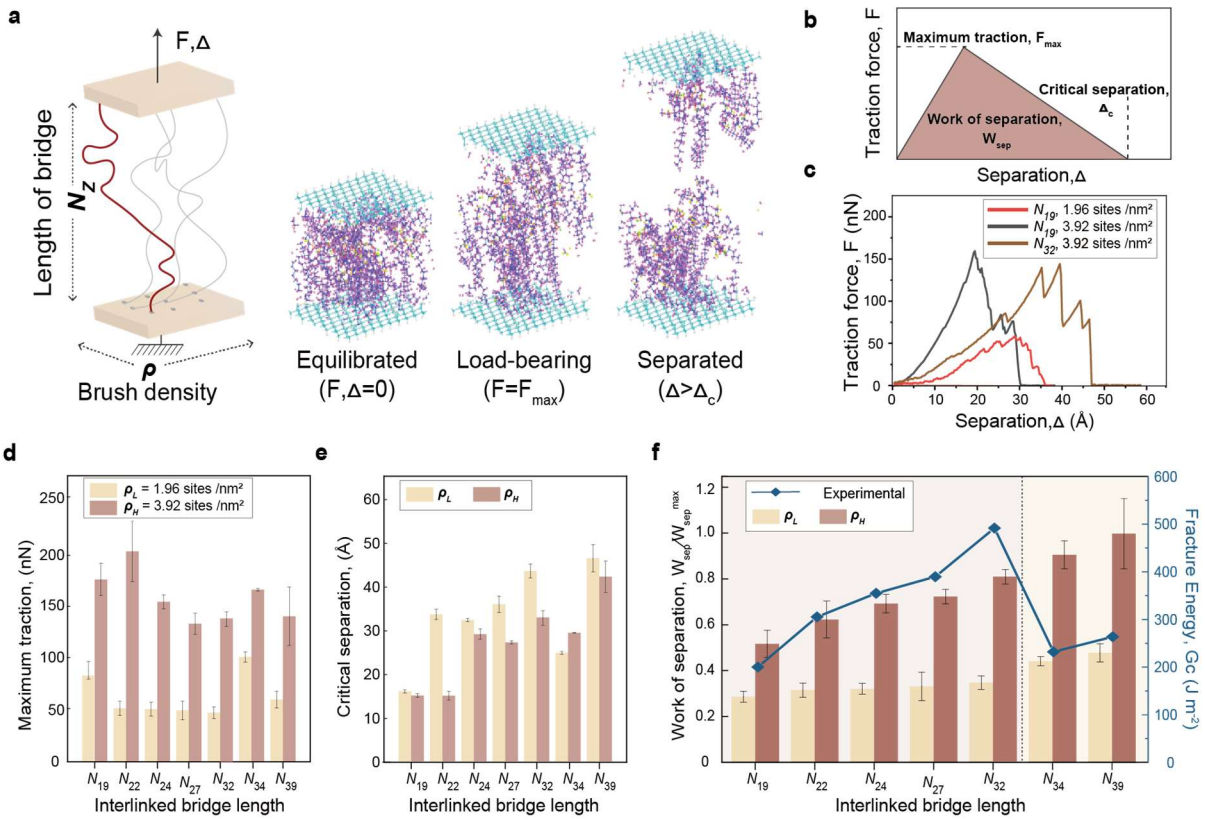


Fig. 4 | Molecular dynamics analysis on the effects of bridge length and brush density. **a**, Schematic of the interlinked molecular interface and representative molecular dynamics (MD) snapshots during a normal separation. The lower support was fixed while the upper support was displaced normal to the interface. **b**, Schematic traction–separation response defining the maximum traction (F_{max}), critical separation (Δ_c), and the work of separation (W_{sep}). **c**, Representative traction–separation responses obtained from the MD simulations for selected bridge lengths and brush densities. **d**, Maximum traction as a function of bridge length at different brush densities (ρ_L=1.96 sites nm^{-2}, ρ_H=3.92 sites nm^{-2}). **e**, Critical separation as a function of bridge length at different brush densities. **f**, calculated normalized work of separation (W_{sep}) is compared with the experimentally measured fracture energy (G_c). The experimental values up to N_{32} are consistent with the high-density simulation, whereas those at longer bridge lengths become more consistent with the low-density

simulation. Error bars represent the standard deviation across three repeated separation trajectories initiated from the same equilibrated configuration.

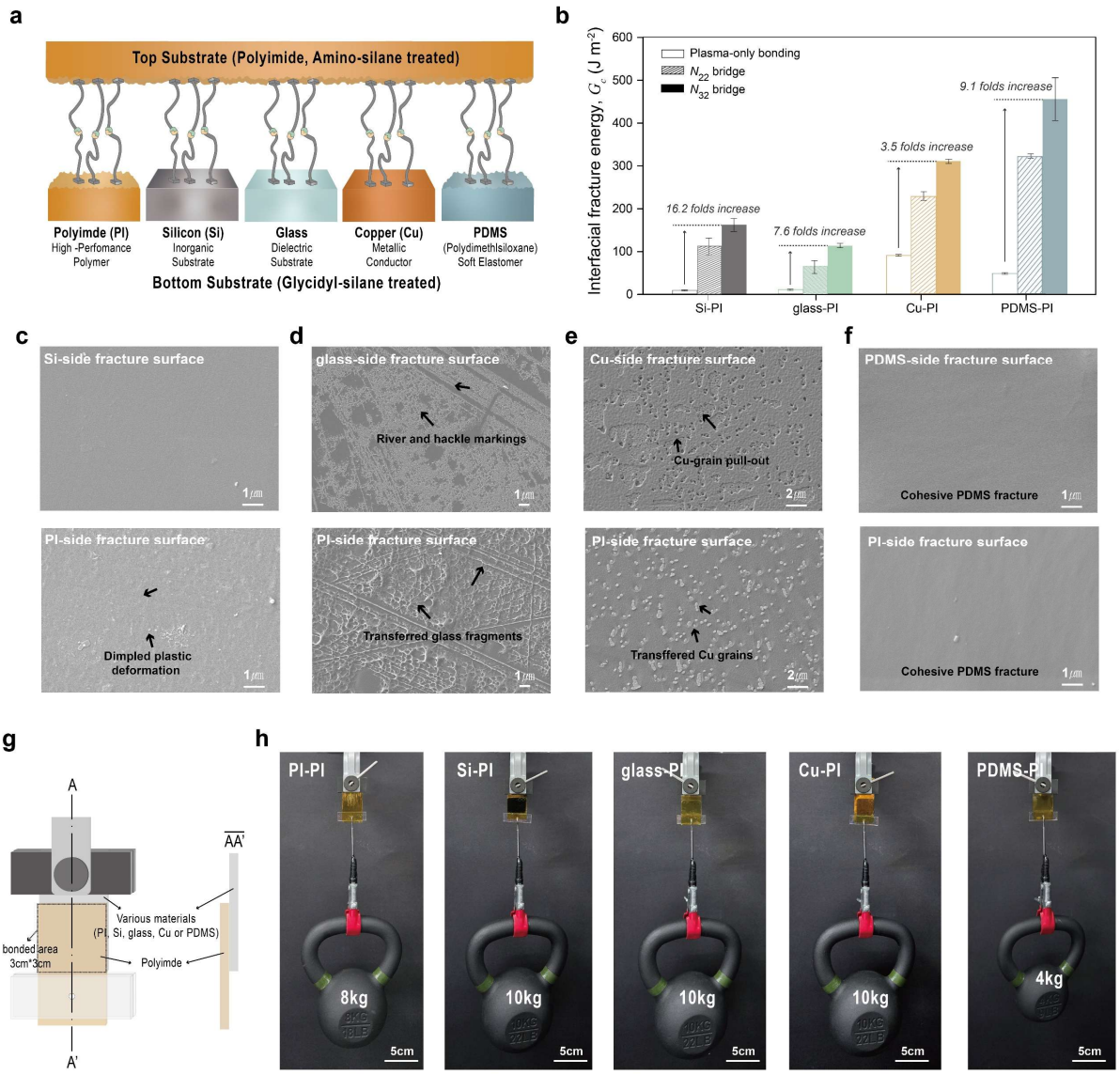


Fig. 5 | Fracture behavior across molecularly bridged heterogeneous interfaces

a, Schematic of the molecular-bridging strategy used to bond amino-silane-functionalized PI to glycidyl-silane-functionalized PI, Si, glass, Cu and PDMS. A_{12}/G_9 and A_{17}/G_{14} pairs were used to form N_{22} and N_{32} molecular bridges, respectively. PI, Si, glass and Cu were bonded at 180 °C under 3 kPa for 1 h, whereas PDMS was bonded at 90 °C under 3 kPa for 1 h. **b,** Interfacial fracture energies (G_c) of Si–PI, glass–PI, Cu–PI and PDMS–PI interfaces. Fold increases above the bars are relative to the corresponding plasma-only controls. Data are mean ± s.d. (n=5). **c–f,** Representative SEM images of paired fracture surfaces from N_{32}-

bridged Si–PI, glass–PI, Cu–PI and PDMS–PI interfaces after a peeling test, respectively, showing dimpled PI deformation, transferred glass fragments, transferred Cu grains, and cohesive PDMS fracture. Corresponding pristine surfaces are shown in Supplementary Fig. 21, and material transfer was further corroborated by EDS (Supplementary Fig. 22). **g,** Schematic of the static load-bearing test using a bonded area of 3 cm × 3 cm. **h,** Photographs of N_{32}-bridged PI–PI, Si–PI, glass–PI, Cu–PI and PDMS–PI joints supporting loads of 8, 10, 10, 10 and 4 kg, respectively, for 1 h.

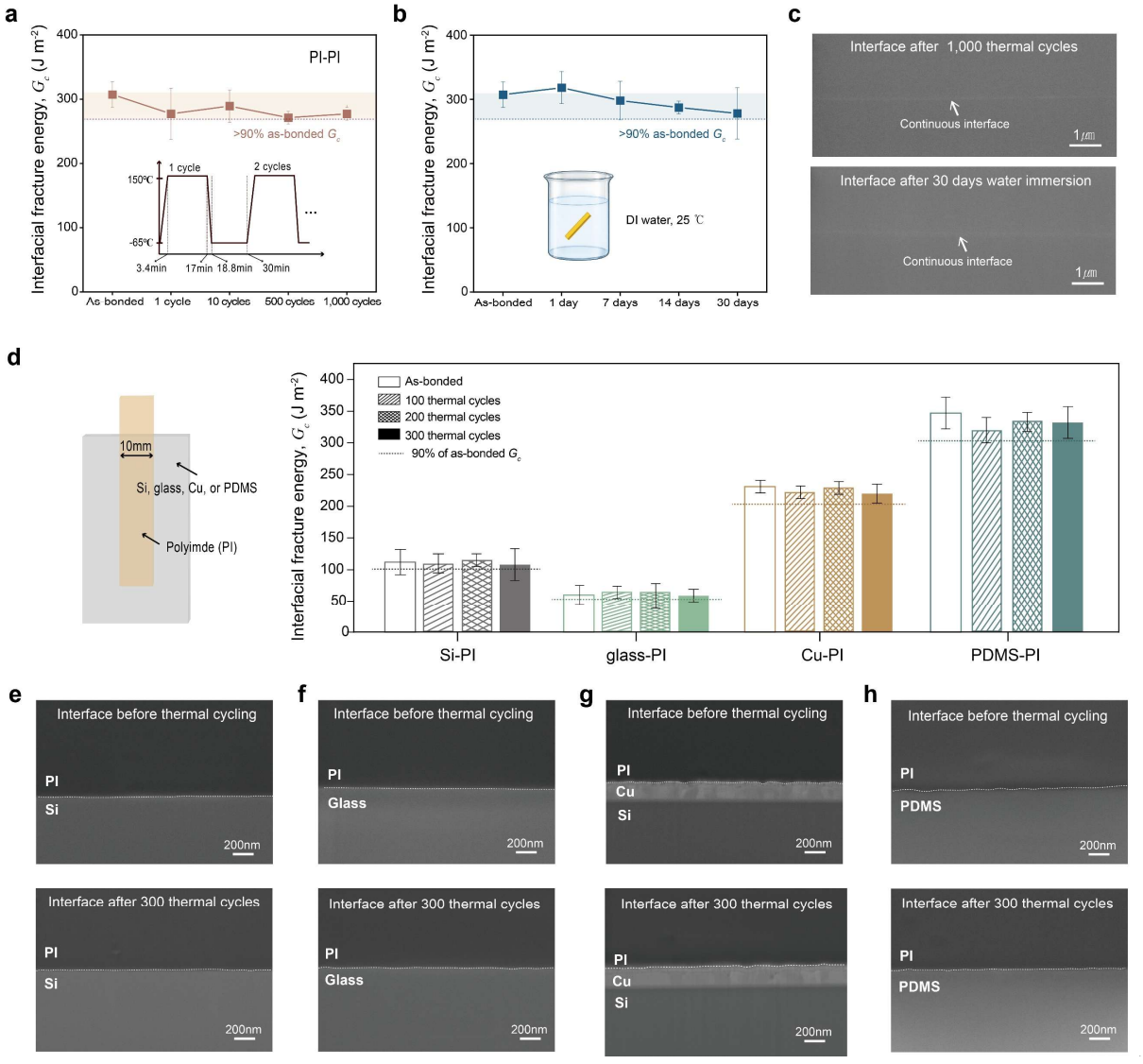


Fig. 6 | Environmental reliability of molecularly bridged homogeneous and heterogeneous interfaces

a, Interfacial fracture energy (G_c) of N_{22}-bridged PI–PI interfaces after thermal cycling between −65°C and 150 °C for up to 1,000 cycles. Inset, thermal-cycling temperature profile. **b,** G_c of N_{22}-bridged PI–PI interfaces after immersion in deionized water at 25 °C for up to 30 days. Inset, schematic of the water-immersion condition. **c,** Representative focused ion beam scanning electron microscopy (FIB–SEM) cross-sections of N_{22}-bridged PI–PI interfaces after 1,000 thermal cycles and 30 days of water immersion, showing continuous

855 interfaces without obvious interfacial gaps or delamination. The corresponding as-bonded PI–
856 PI interface is shown in Supplementary Fig. 25. **d,** Left, schematic of the specimen geometry
857 used for thermal-cycling tests of heterogeneous interfaces. Right, interfacial fracture energy
858 (G_c) of N_{22}-bridged Si–PI, glass–PI, Cu–PI and PDMS–PI interfaces after thermal cycling
859 between −40°C and 125 °C. Data are presented as mean ± s.d. from $n = 5$. **e–h,** Representative
860 FIB–SEM cross-sections of N_{22}-bridged Si–PI, glass–PI, Cu–PI and PDMS–PI interfaces,
861 respectively, before thermal cycling and after 300 thermal cycles. The interfaces remain
862 continuous after cycling.

863

Supplementary Files

This is a list of supplementary files associated with this preprint. Click to download.

- SupplementaryMovie2.mp4
- SupplementaryInformation.pdf
- SupplementaryMovie1.mp4